EPR Study of the Astaxanthin *n*-Octanoic Acid Monoester and Diester Radicals on Silica–Alumina

A. Ligia Focsan,*[†,‡] Michael K. Bowman,[‡] Julia Shamshina,[‡] Matthew D. Krzyaniak,[‡] Adam Magyar,[‡] Nikolay E. Polyakov,[§] and Lowell D. Kispert*[‡]

[†]Department of Chemistry, Valdosta State University, Valdosta, Georgia 31689, United States
[‡]Department of Chemistry, The University of Alabama, Tuscaloosa, Alabama 35487-0336, United States
[§]Institute of Chemical Kinetics & Combustion, Institutskaya Str. 3, 630090, Novosibirsk, Russia

Ⓢ *Supporting Information*

ABSTRACT: The radical intermediates of the *n*-octanoic monoester and *n*-octanoic diester of astaxanthin were detected by pulsed EPR measurements carried out on the UV-produced radicals on silica–alumina artificial matrix and characterized by density functional theory (DFT) calculations. Previous Mims ENDOR for astaxanthin detected the radical cation and neutral radicals formed by proton loss from the C3 (or C3′) position and from the methyl groups. Deprotonation of the astaxanthin neutral radical formed at the C3 (or C3′) position resulted in a radical anion. DFT calculations for astaxanthin showed that the lowest energy neutral radical forms by proton loss at the

n-octanoic acid diester

Favored neutral radical formed by H⁺ loss from the methyl group of the cyclohexene end of the radical cation

C3 (or C3′) position of the terminal ring followed by proton loss at the methyl groups of the polyene chain. Contrary to astaxanthin where proton loss can occur at either end of the symmetrical radical, for the diester of astaxanthin, this loss is prevented at the cyclohexene ends and is favored for its methyl groups. The monoester of astaxanthin, however, allows formation of the neutral radical at C3′ and prevents its formation at the opposite end where the ester group is attached. At the terminal ring without the ester group attached, migration of proton from hydroxyl group to carbonyl group facilitates resonance stabilization, similarly to already published results for astaxanthin. However, cw EPR shows no evidence of a monoester radical anion formed. This study suggests the different radicals of astaxanthin and its esters that would form in a preferred environment, either hydrophobic or hydrophilic, depending on their structure.
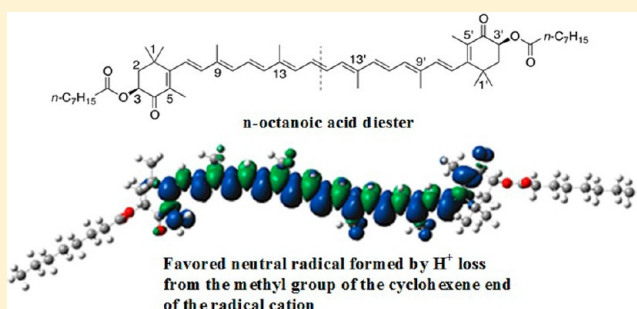
INTRODUCTION

Under intense light, photosynthetic organisms gather excess light and quench what is not needed, thus avoiding unwanted photochemical damage. The carotenoids zeaxanthin and lutein have a direct role in the quenching chlorophyll excited state, while epoxy-containing carotenoids like violaxanthin and 9′-*cis* neoxanthin do not.[1] Holt et al.[2] showed that a charge-transfer state formed between zeaxanthin (Zea) and chlorophyll (Chl) quenches Chl excited singlet states, transiently producing radical cation Zea[•+] and radical anion Chl[•−]. This charge-transfer quenching mechanism has also been observed in light harvesting minor complexes CP24, CP26, and CP29.[3−5] Recently, an additional step has been proposed:[6] proton loss from Zea[•+] to form the #Zea[•] neutral radical (proton loss indicated by #) which could act as a radical trap and be a very efficient quencher of chlorophyll excited states. Lutein radical cation could give a similar quenching reaction because proton loss can readily occur from its cyclohexene ends, but the terminal rings of 9′-*cis* neoxanthin or violaxanthin radical cations cannot readily lose a proton.[6,7] Furthermore, it has been noted[7] that in some cellular systems loss of protons at the terminal rings of the carotenoid is favored because the end of the carotenoid is located in the

hydrophilic pocket. This proton loss in hydrophilic media at pH 4−7 is possible because the pK_a of carotenoid radical cations lies between 4 and 7. For some carotenoids, structural constraints prevent such a proton loss from occurring.[6,7]

A photoprotective role has been suggested for the carotenoid astaxanthin. Under high light and often with excess metal ions, astaxanthin accumulates in a huge amount (up to 30 mg/g) in some unicellular green algae[8−12] and this accumulation is generally thought[11] to be a survival strategy under photooxidative and salt stress. *Haematococcus pluvialis* algae accumulates 1% of cell mass as carotenoids: 70% monoesters of astaxanthin, 10% diesters of astaxanthin, and 5% astaxanthin, with approximately 5% each of lutein, canthaxanthin, and β-carotene.[13] The presence of the 70% monoester versus 10% diester suggests a preferred orientation of carotenoid in the cell of *Haematococcus pluvialis* algae, with one hydrophobic and one hydrophilic end.
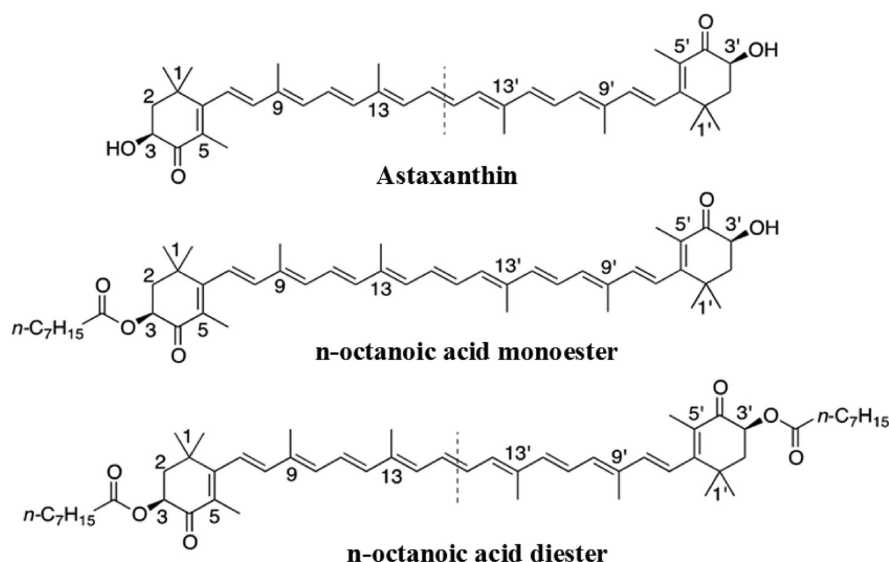
We undertook an EPR study to examine the formation and properties of neutral radicals derived from the monoester and

Chart 1. The Structures of the Carotenoids Astaxanthin, *n*-Octanoic Acid Monoester, and *n*-Octanoic Acid Diester and the Numbering System Used for Each in This Study

the diester of astaxanthin on silica–alumina. Proton loss in astaxanthin can occur at either end of the symmetrical radical cation.[14] DFT calculations for astaxanthin determined[14] that proton loss at the terminal rings of the radical cation was favored over loss from the methyl groups of the polyene chain. Deprotonation at C3, and by symmetry at C3′, resulted in the lowest energy neutral radical #Ast•(3)b due to resonance stabilization upon hydroxyl proton migration to the carbonyl group. The pulsed EPR measurements detected the UV-produced radical cation and an equal amount of neutral radicals, as well as a measurable amount of a radical anion due to deprotonation of the hydroxyl group of either neutral radical #Ast•(3)a (defined as proton loss at C3) or #Ast•(3)b (defined as proton loss at C3 followed by hydroxyl proton migration to the carbonyl group) supported on silica–alumina or molecular sieves at 77 K.[14] We also reported a large $K_1 = 23\,000$ M^{-1} stability constant for the mono calcium salt complex with astaxanthin. Upon complexation, the electron withdrawing effect of the positively charged metal ion decreases the electron density on the cyclohexene ring on the opposite end of the carotenoid. This increases the affinity of astaxanthin facilitating proton loss and the formation of monoesters. In the present study, DFT calculations and pulsed EPR measurements were performed for the *n*-octanoic acid monoester and diester of astaxanthin to determine where and in what order proton loss occurs for the monoester and diester, whether a monoester radical anion is formed, and whether there is evidence in the cw EPR spectrum of the large DFT-predicted couplings for the neutral radicals #Ast•(3)a. The structures and numbering system used in this paper for astaxanthin, *n*-octanoic acid monoester, and *n*-octanoic acid diester are given in Chart 1.

■ **EXPERIMENTAL SECTION**

Chemical and Sample Preparation. Astaxanthin was purchased from Sigma (99%) and stored at −14 °C in a desiccator. The sample purity was determined by ^{1}H NMR (360 MHz, CDCl$_3$). No unaccounted NMR lines were observed, and the purity was estimated to be better than 98%. The deuterated solvent CDCl$_3$ (Cambridge Isotope Laboratories) was used as supplied. Anhydrous methylene chloride (CH$_2$Cl$_2$, Aldrich) was

stored under nitrogen in a drybox and used without further purification.

Esters of astaxanthin, *n*-octanoic acid monoester, and *n*-octanoic acid diester were synthesized according to Fukami et al.[15] Purification was achieved on a chromatography column using Silicycle silicagel.

Silica–alumina (Al$_2$O$_3$ 13%, Aldrich) was activated by heating at 550 °C for 5 h in air in an open ceramic "boat", cooled to 50 °C, and stored in a desiccator as previously carried out.[6,7]

Carotenoid (1.7 mg of astaxanthin, 2.3 mg of *n*-octanoic acid monoester, or 2.6 mg of *n*-octanoic acid diester of astaxanthin) solutions in 0.5 mL of CH$_2$Cl$_2$ (6×10^{-3} M) were degassed in 4 mm quartz EPR tubes by three freeze–pump–thaw cycles. Fresh activated silica–alumina was then added to the carotenoid solution in the EPR tube until the carotenoid solution became clear. The solvent was evaporated under reduced pressure, and then, the tube was evacuated and sealed. EPR samples were stored at 77 K and UV-irradiated with a 200 W Xe lamp at a distance of 10 cm for 5 min according to previously published papers.[6,7,14]

NMR Measurements. NMR spectra were collected utilizing a Bruker spectrometer 360 MHz Bruker Avance Spectrometer Bruker/Magnex UltraShield 360 MHz magnet. Spectra were processed using the Mestrec program. 0.7 mg of carotenoid (astaxanthin, *n*-octanoic acid monoester, or *n*-octanoic acid diester of astaxanthin) in 0.5 mL CDCl$_3$ solutions were prepared. Figure 1 provides the ^{1}H NMR spectra of astaxanthin, its monoester, and diester, confirming the structures of prepared ester derivatives.

EPR and ENDOR Measurements. Pulsed ENDOR experiments were carried out with a Bruker ELEXSYS E-680W/X FT/CW pulse X-band EPR spectrometer with an ENI A-500 RF power amplifier using the Mims ($\pi/2$-τ-$\pi/2$-T-$\pi/2$-τ-echo) pulse sequences with a RF π-pulse applied during the delay time T.[16] Pulsed ENDOR simulations were performed using the Sim-Bud/SpecLab programs[17] using DFT-generated hyperfine coupling tensors.

DFT Calculations. All DFT calculations were done with the Gaussian 03[18] and Gaussian 09[19] program packages on the Cray XD1 computer at the Alabama Supercomputer Center.
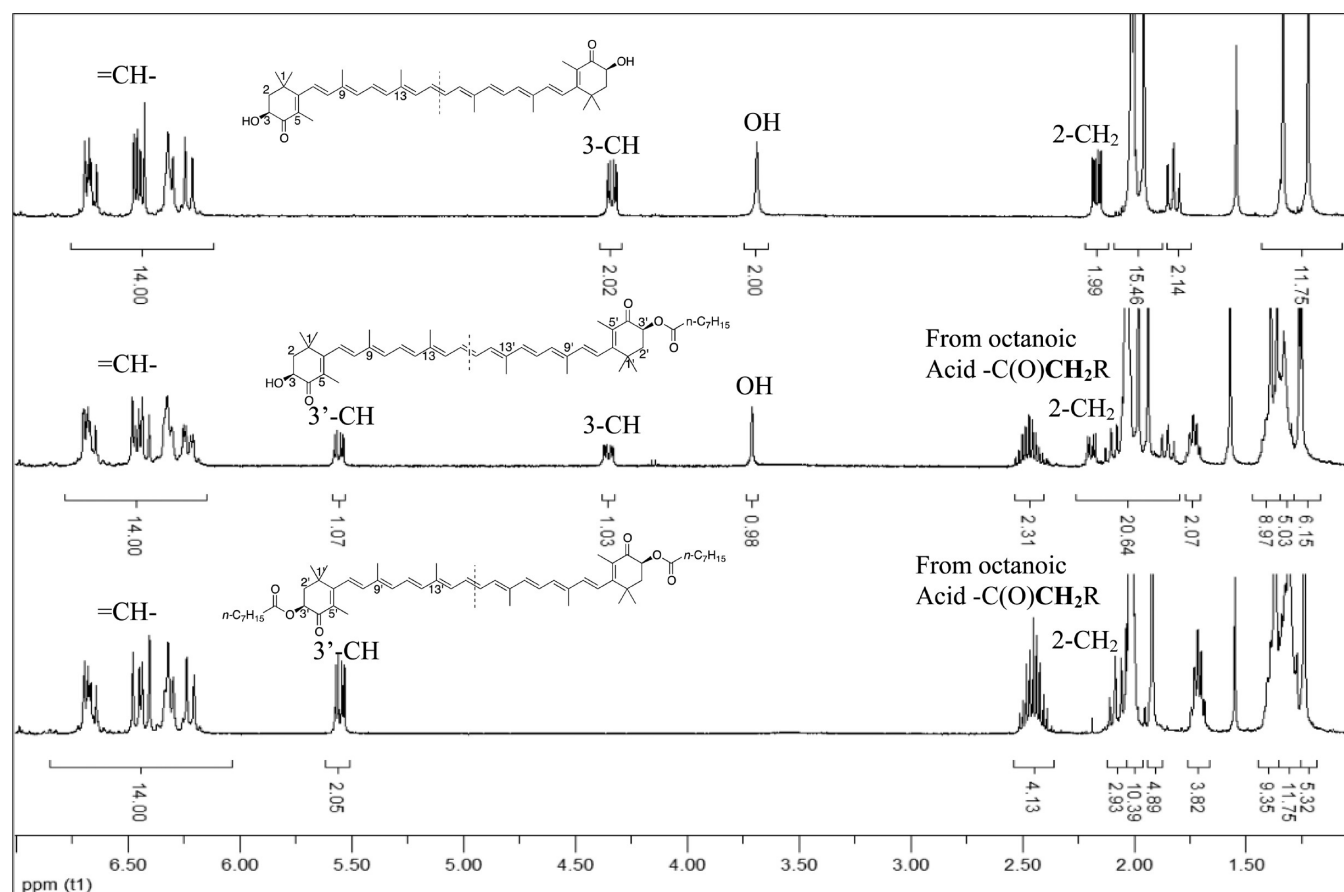
Figure 1. The NMR spectrum of astaxanthin (upper) and the *n*-octanoid acid monoester and diester (lower) confirming the structures of prepared ester derivatives.

Geometries were optimized at the B3LYP/6-31G** level,[20,21] which we have previously shown[22] to be suitable for predicting the geometry of β-carotene based radicals. Single-point calculations at these geometries were used to predict ENDOR hyperfine couplings at the B3LYP level with the TZP basis set from Ahlrich's group.[23] This basis set has been shown to give good NMR chemical shifts[24] and EPR parameters that agree well with the experimental data for carotenes.[6,22] The proton hyperfine couplings calculated with this method are within 0.5 MHz of the experimental couplings, whereas other levels of theory give values that differ by as much as a factor of 2.[22] The isotropic and anisotropic proton coupling tensors for the three carotenoids studied are given in the Supporting Information in Tables S1−S24. The unpaired spin densities defined as the difference in the α and β spin densities were obtained using the AGUI interface (Semichem, Inc.)[25] from the wave functions and spin densities produced by Gaussian 09.

■ RESULTS

Figure 2 presents the echo-detected field swept EPR spectra of *n*-octanoic acid monoester and *n*-octanoic acid diester radicals of astaxanthin supported on silica−alumina. The two spectra overlap each other, implying that similar radicals are formed for the monoester and diester, also consistent with the Mims ENDOR spectra performed at τ = 200 ns presented in Figure 3. Previous Mims ENDOR for astaxanthin at τ = 200 ns showed significant evidence of a radical anion (formed by deprotonation of the hydroxyl group of either neutral radical #Ast•(3)a or #Ast•(3)b) that built up rather intense lines in the middle of the spectrum.[14]
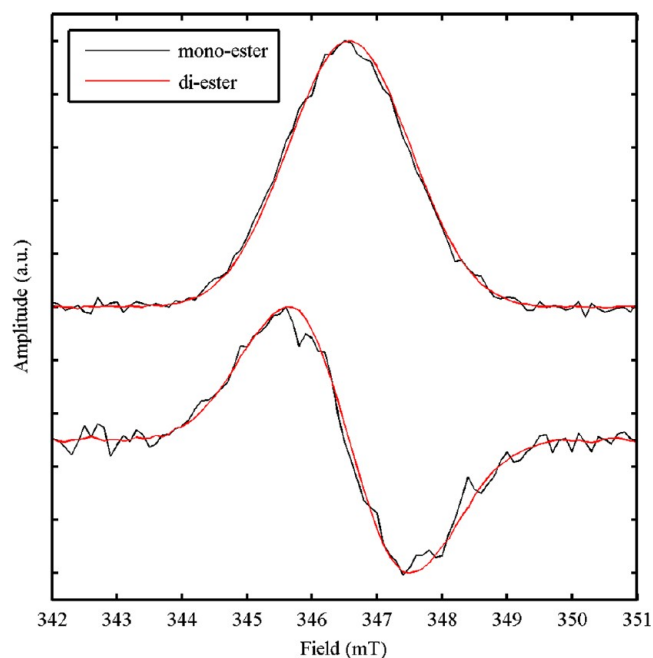

Figure 2. The echo detected, field swept EPR spectrum of the *n*-octanoic acid monoester (black) and diester (red) of astaxanthin radicals supported on silica−alumina: absorption (top) and pseudomodulated presentation (bottom).

However, there are no such intense lines in the Mims ENDOR spectrum of the monoester and diester, the relative intensities
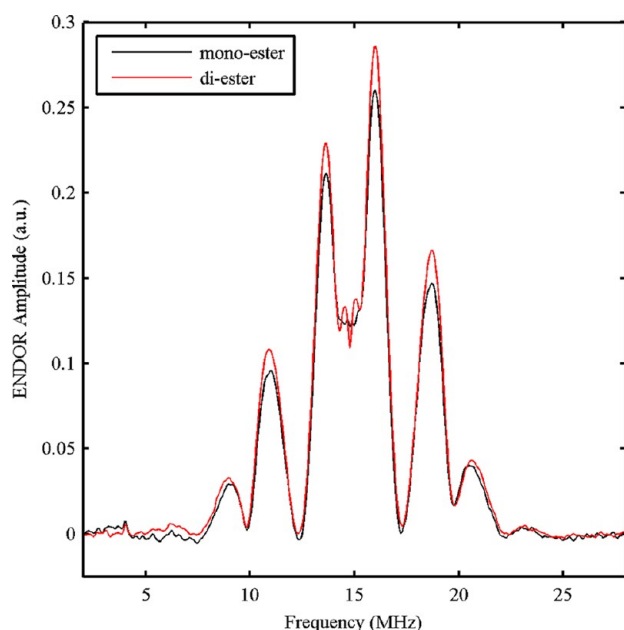
Figure 3. Mims ENDOR spectra of the astaxanthin *n*-octanoic acid monoester and diester at 9.73 GHz and 3465 G, with τ = 200 ns.

of the peaks at about 18 and 16 MHz being in a ratio of 1:2 (Figure 3) rather than 1:3 in the astaxanthin spectrum (Figure 8 in ref 14). This indicates that the radical anion is not formed in a detectable quantity for the monoester. Large couplings (18.62 and 75.89 MHz in Table S2, Supporting Information) were predicted by DFT for neutral radical #Ast•(3)a[14] and for #mono-Ast•(3 or 3′)a (22.03 and 89.58 MHz in Table S10 or 18.73 and 75.70 MHz in Table S11, Supporting Information) or #di-Ast•(3) (22.35 and 98.80 MHz in Table S21, Supporting Information) which were not detected by EPR.

A scheme of the possible proton loss from the carotenoid radical cations on silica−alumina upon irradiation is given in Figure 4 for astaxanthin. In the absence of light, electron transfer from astaxanthin to the silica−alumina matrix occurs and the radical cation is formed.[14,26] Upon UV irradiation, loss of H+ from radical cations gives rise to neutral radicals.

On the basis of this as a model, the structures and relative energies of radical cations and neutral radicals of astaxanthin, *n*-octanoic acid monoester, and *n*-octanoic acid diester were calculated by DFT. The relative energies $\Delta E(n)$ are given in Table 1 for neutral radicals (# indicates proton loss at position *n* of the radical cation). The relative energy varies inversely to the delocalization length, and usually, the most favorable deprotonation takes place at a site that extends the unpaired spin delocalization length.

Proton loss from terminal rings at C3 (or C3′) where the ester is attached was investigated for the *n*-octanoic acid monoester and diester of astaxanthin. It was found that proton migration from hydroxyl group to carbonyl group facilitates resonance stabilization of molecules at both ends of astaxanthin and at the primed end of the monoester (see Chart 2). The adjacent carbonyl group makes astaxanthin neutral radical #Ast•(3)b (or #Ast•(3′)b by symmetry) substantially more stable than the monoester neutral radical #mono-Ast•(3′)b which is destabilized by the electronegative ester at the unprimed end (see Chart 2). This explains why the neutral radicals #Ast•(3)a or #mono-Ast•(3′)a are not observed by EPR.

Neutral radicals #Ast•(3)b of astaxanthin and #mono-Ast•(3′)b of monoester have the lowest energy among all neutral radicals (see Table 1). Contrary to astaxanthin where proton loss can occur at C3 (or C3′) at either end of the symmetrical radical, and to the monoester where proton loss occurs at one end at C3′, for the diester of astaxanthin, this loss at C3 (or C3′) is prevented and is most favorable at the methyl group attached to the C5 (or 5′) position.

For astaxanthin, the next energetically favorable neutral radicals are those formed by proton loss from the methyl groups attached to positions C5 (or 5′), C9 (or 9′), and C13 (or 13′), namely, #Ast•(5 or 5′), #Ast•(9 or 9′), and #Ast•(13 or 13′), which are 13.74, 14.03, and 15.89 kcal/mol higher, respectively (see Table 1). By comparison, for diester where the hydroxyl groups are replaced at both ends by ester groups, the lowest energy structure is formed by proton loss from the methyl group attached to C5 (or 5′), with proton loss from methyl groups attached to C9 (or 9′) and C13 (or 13′), 3.75 and 4.80 kcal/mol higher, respectively (see Table 1). On the other hand, breaking the symmetry to form the monoester does not change the relative energy increase from C(5 or 5′) to C(9 or 9′) to C(13 or 13′), with C(5′) being slightly more favorable lower than C(5) by ∼5 kcal/mol (see Table 1).

Unpaired Spin Density Distribution. The radical cations and neutral radicals of the three carotenoids in this study exhibit a spin pattern with alternating positive (blue) and negative (green) lobes, as seen in Figure 4. The radical cation has the unpaired spin distributed all along the polyene chain, while for the neutral radicals the length of the unpaired spin density decreases with decreasing conjugation length (Figure 4). The length *N* over which the unpaired spin density is distributed increases monotonically as the relative energy decreases. The longer the conjugation length, the more distributed is the unpaired spin density and the more stable the radical, reducing the likelihood of further reactions. On the contrary, localized unpaired spin density gives rise to unstable radicals that are not observed in the EPR spectra. For example, astaxanthin neutral radical #Ast•(3)b has the lowest energy among the neutral radicals and a conjugation length of about 25−27 carbon atoms, and is more stable than #Ast•(5) with a conjugation length of 23−25 carbon atoms, more stable than #Ast•(9) with 19−21 C atoms, and more stable than Ast•(13) with 15−17 carbon atoms (see Table 1 and Figure 4). This pattern is repeated in its esters (Figures 5 and 6).

Proton loss at C3 (where the ester group is attached) of the monoester radical cation generates the neutral radical #mono-Ast•(3)a with high energy (27.19 kcal/mol), large couplings, and a conjugation length of 16−18 carbon atoms. On the contrary, proton loss at primed position C3′ for #mono-Ast•(3′)a gives low energy (10.16 kcal/mol), a long conjugation length of 22−24 carbon atoms, and smaller couplings. Diester neutral radical #di-Ast•(3 or 3′)a gives the highest energy (8.68 kcal/mol), a conjugation length of 16−18 carbon, and large couplings, undetected with EPR. However, radical #Ast•(3)b of astaxanthin gives the lowest energy structure with the longest conjugation length of 25−27 carbon atoms due to stabilization of negative charge by the carbonyl group and proton migration (see Chart 2, Scheme 1). Similarly, neutral radical #mono-Ast•(3′)b formed by proton loss at position C3′ and proton migration to the carbonyl group gives the lowest energy structure and the same conjugation length (see Table 1). Such a radical is not possible to form for diester.

For neutral radical #mono-Ast•(3′OH), a proton was removed from the hydroxyl group (see Figure 5). This structure has relatively high energy with unpaired spin localized around the
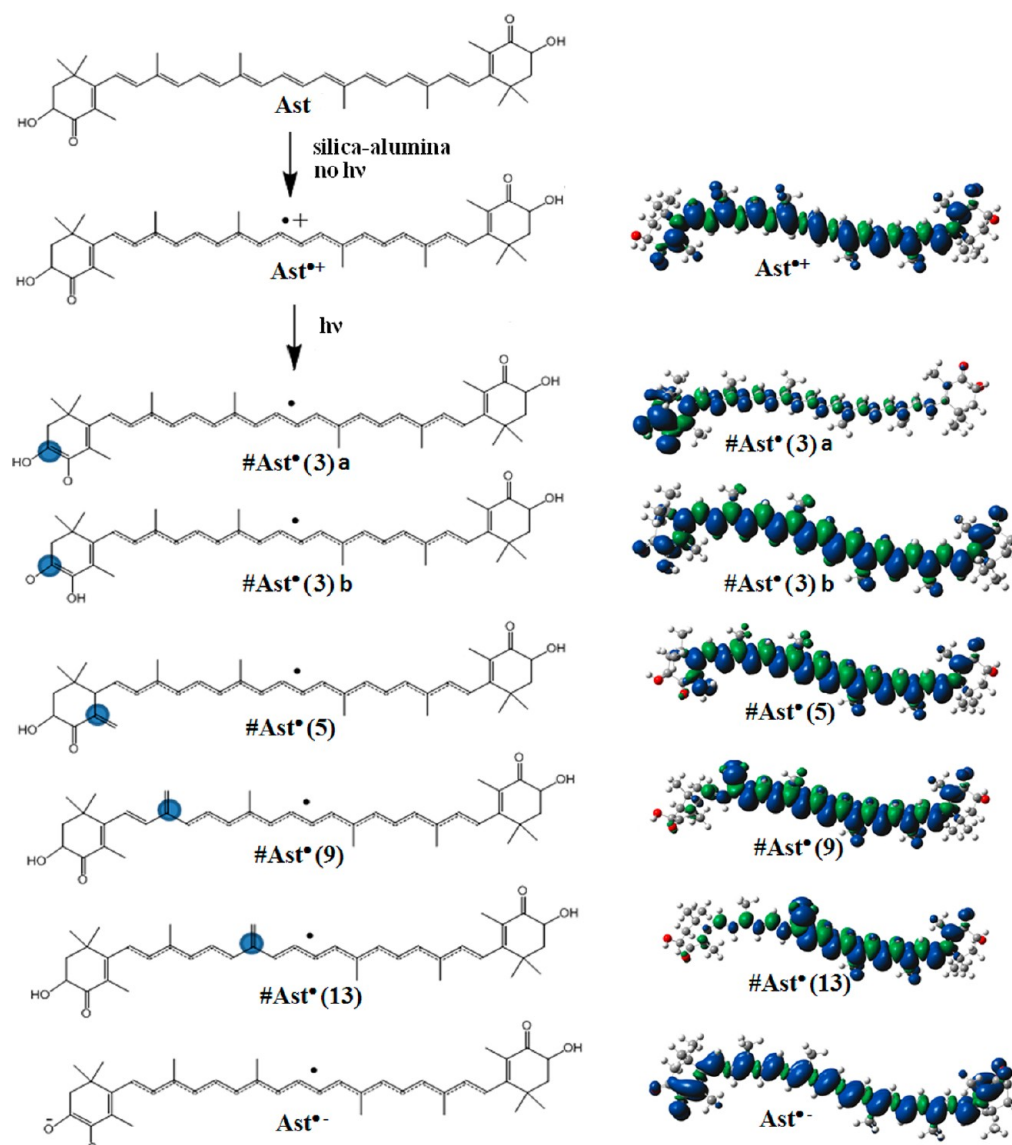
Figure 4. Unpaired spin distribution for astaxanthin radicals Ast$^{\bullet+}$, #Ast$^{\bullet}$(3)a, #Ast$^{\bullet}$(3)b, #Ast$^{\bullet}$(5), #Ast$^{\bullet}$(9), #Ast$^{\bullet}$(13), and Ast$^{\bullet-}$ using the numbering system in Chart 1 (adapted from Scheme 2 in ref 14).

**Table 1. DFT-Calculated Relative Energies $\Delta E(n)$ of Carotenoid Neutral Radicals[a]**

carotenoid unprimed positions	$\Delta E(3)a$	$\Delta E(3)b$	$\Delta E(5)$	$\Delta E(9)$	$\Delta E(13)$
astaxanthin	4.69 (22−24)	0 (25−27)	13.74 (23−25)	14.03 (19−21)	15.89 (15−17)
monoester	27.19 (16−18)	not possible	19.10 (23−25)	22.10 (19−21)	23.59 (15−17)
diester	8.68 (16−18)	not possible	0 (23−25)	3.75 (19−21)	4.80 (15−17)
carotenoid primed positions	$\Delta E(3')a$	$\Delta E(3')b$	$\Delta E(5')$	$\Delta E(9')$	$\Delta E(13')$	$\Delta E(3'OH)$
astaxanthin	4.69 (22−24)	0 (25−27)	13.74 (23−25)	14.03 (19−21)	15.89 (15−17)	35.62 (4−6)
monoester	10.16 (22−24)	0 (25−27)	14.41 (23−25)	22.27 (19−21)	23.64 (15−17)	32.17 (4−6)
diester	8.68 (16−18)	not possible	0 (23−25)	3.75 (19−21)	4.80 (15−17)	not possible

[a]n indicates the position from which the proton was lost (kcal/mol); delocalization length N is given under each $\Delta E(n)$ value and indicated within parentheses. Note: $\Delta E(n)$ is calculated relative to the energy minimum; delocalization is estimated by counting the number of C atoms over which significant spin (>0.002) is delocalized in Figures 2−5.

primed ring (4−6 carbon atoms), giving large couplings and zero couplings for the rest of the molecule (see Table S13, Supporting Information). A similar radical structure is formed for the corresponding astaxanthin neutral radical #Ast$^{\bullet}$(3′OH)

Chart 2. Resonance Stabilization for Astaxanthin (Scheme 1) and Monoester (Scheme 2)[a]
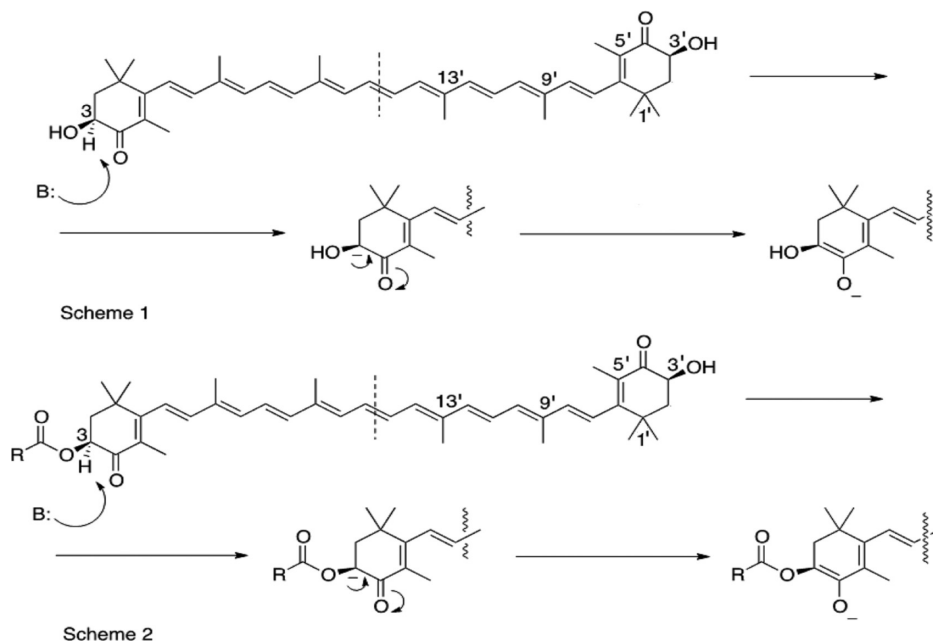
Scheme 1

Scheme 2

[a]In Scheme 1, B: represents a base that removes a proton from position C3 producing an anion and subsequent proton migration to carbonyl group generating the neutral radical #Ast•(3)b and by symmetry #Ast•(3′)b. In Scheme 2, after removal of the proton at position C3 by the base B: at the unprimed (ester) end, a negative charge is generated which simultaneously destabilizes the primed end and forms a monoester neutral radical #mono-Ast•(3′)b which is less stable than #Ast•(3′)b.
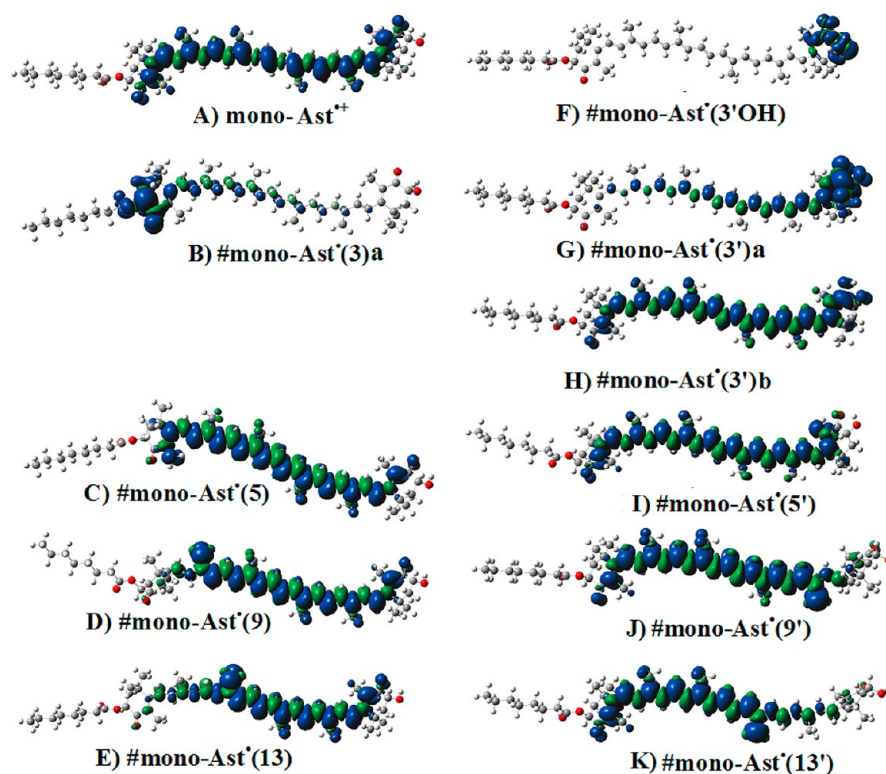

Figure 5. Unpaired spin distribution for astaxanthin *n*-octanoic acid monoester radicals (A) mono-Ast•+, (B) #mono-Ast•(3)a, (C) #mono-Ast•(5), (D) #mono-Ast•(9), (E) #mono-Ast•(13), (F) #mono-Ast•(3′OH), (G) #mono-Ast•(3′)a, (H) #mono-Ast•(3′)b, (I) #mono-Ast•(5′), (J) #mono-Ast•(9), and (K) #mono-Ast•(13′) using the numbering system in Chart 1.

(see Table S4, Supporting Information). There is no such radical for diester.

Unpaired spin density patterns for the three carotenoids are compared in Figure 7. The unpaired spin density increases in the direction from where the proton was lost. For example, proton loss from the methyl group attached to position C5 generates more stable radicals with longer conjugation length (23−25 carbon atoms), followed by neutral radicals formed by proton
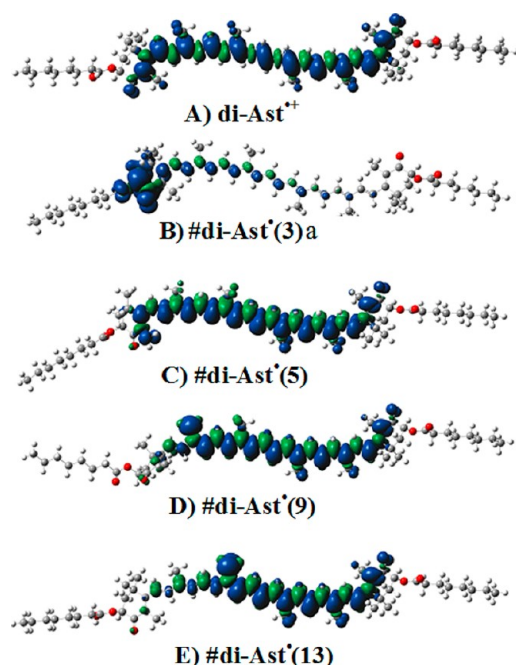
Figure 6. Unpaired spin distribution for astaxanthin *n*-octanoic acid diester radicals (A) di-Ast$^{\bullet+}$, (B) #di-Ast$^{\bullet}$(3)a, (C) #di-Ast$^{\bullet}$(5), (D) #di-Ast$^{\bullet}$(9), and (E) #di-Ast$^{\bullet}$(13) using the numbering system in Chart 1.

loss from the methyl group attached to position C9 (19−21 carbon atoms) and neutral radicals formed by proton loss from the methyl group attached to position C13 (15−17 carbon atoms). Neutral radicals formed by proton loss at the methyl groups attached to the primed positions (C5′, C9′, and C13′) have similar patterns with those corresponding to the unprimed positions (not shown here).

Unpaired spin density distributions are also correlated with the proton couplings. For comparison, the proton coupling tensors for astaxanthin radicals are given in Tables S1−S8 (Supporting Information). The monoester proton coupling tensors are given in Tables S9−S19, and the proton coupling tensors for the diester are given in Tables S20−S24 (Supporting Information).

Table 2. DFT-Calculated Isotropic Coupling Constants of Radical Cations of Astaxanthin, Monoester, and Diester

position	number of protons	Ast$^{\bullet+}$	mono-Ast$^{\bullet+}$	di-Ast$^{\bullet+}$
1	3	−0.05	−0.05	−0.05
	3	0.33	0.32	0.33
1′	3	0.01	−0.05	−0.05
	3	0.33	0.36	0.33
5	3	5.05	5.39	5.35
5′	3	4.45	5.35	5.31
9	3	9.17	9.64	9.57
9′	3	9.23	9.62	9.6
13	3	5.62	5.86	5.84
13′	3	6.06	5.83	5.86

Similar isotropic (Table 2) and anisotropic couplings (Tables S1, S9, and S20, Supporting Information) were calculated for the radical cation of astaxanthin Ast$^{\bullet+}$, monoester mono-Ast$^{\bullet+}$, and diester di-Ast$^{\bullet+}$. The radical cation of the mono-Ast$^{\bullet+}$ gives couplings almost identical to those of the di-Ast$^{\bullet+}$ (within ±0.05 difference) and slightly higher than those of Ast$^{\bullet+}$ (see Table 2).

There are no significant differences for the isotropic couplings of the neutral radicals of monoester, diester, and astaxanthin formed by proton loss from position C3 or from the methyl groups (see Tables 3, 4, 5, and 6). However, when comparing the isotropic couplings of the neutral radical of the monoester #mono-Ast$^{\bullet}$(3′)b, with the lowest energy structure, to that of astaxanthin neutral radical Ast$^{\bullet}$(3)b, higher (up to approximately 2.5 MHz difference) isotropic couplings are noted (see Table 7).

When comparing neutral radicals of the monoester formed at opposite rings, for example, couplings for #mono-Ast$^{\bullet}$(3)a versus #mono-Ast$^{\bullet}$(3′)a (Table 8), #mono-Ast$^{\bullet}$(5) versus #mono-Ast$^{\bullet}$(5′)a (Table 9), #mono-Ast$^{\bullet}$(9) versus #mono-Ast$^{\bullet}$(9′) (Table 10), and #mono-Ast$^{\bullet}$(13)a versus #mono-Ast$^{\bullet}$(13′)a (Table 11), we observe similar numerical values and a change in sign.

ENDOR Spectral Simulation. In order to interpret the overlapping powder ENDOR spectra composed of a mixture of carotenoid radicals, containing radical cations and neutral radicals,
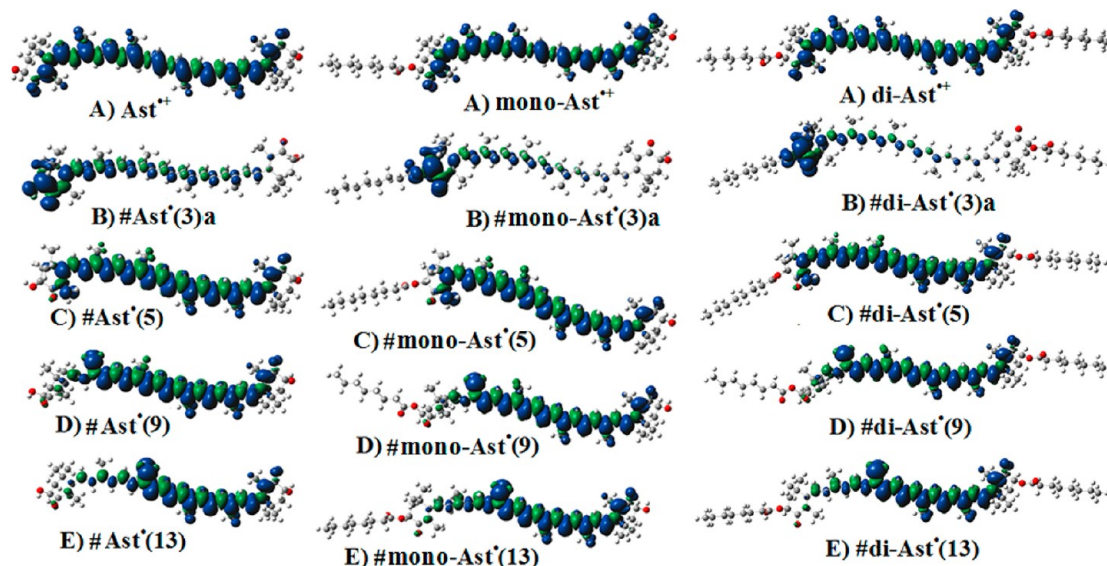

Figure 7. Comparison of the unpaired spin density distribution for astaxanthin, *n*-octanoic acid monoester, and diester for the unprimed positions using the numbering system in Chart 1.

Table 3. DFT-Calculated Isotropic Coupling Constants of Neutral Radical Formed by Proton Loss at Position C3 for Astaxanthin, Monoester, and Diester

position	number of protons	#Ast•(3)a	#mono-Ast•(3)a	#di-Ast•(3)a
1	3	−0.43	−0.54	−0.54
	3	0.09	0.2	0.19
1′	3	0.01	0.02	0.02
	3	0.04	0	0
2	1	18.62	22.03	22.35
	1	75.89	89.58	98.8
5	3	−2.61	0.34	0.32
5′	3	0.38	0.14	0.11
9	3	−1.2	−0.74	−0.81
9′	3	0.92	0.33	0.34
13	3	−0.78	−0.53	−0.6
13′	3	1.03	0.49	0.54

Table 4. DFT-Calculated Isotropic Coupling Constants of Neutral Radical Formed by Proton Loss at the Methyl Group Attached to Position C5 for Astaxanthin, Monoester, and Diester

position	number of protons	#Ast•(5)	#mono-Ast•(5)	#di-Ast•(5)
1	3	0.46	0.38	0.29
	3	−0.1	−0.16	−0.11
1′	3	0.01	0.40	0.47
	3	0.04	0.10	0.12
5	1	−2.36	−3.25	−2.33
	1	−2.67	−3.59	−2.61
5′	3	3.71	3.35	3.33
9	3	−4.62	−5.44	−4.15
9′	3	10.09	9.01	9.71
13	3	−7.53	−8.2	−6.95
13′	3	14.05	12.99	13.71

Table 5. DFT-Calculated Isotropic Coupling Constants of Neutral Radical Formed by Proton Loss at the Methyl Group Attached to Position C9 for Astaxanthin, Monoester, and Diester

position	number of protons	#Ast•(9)	#mono-Ast•(9)	#di-Ast•(9)
1	3	−0.01	−0.02	−0.02
	3	−0.09	−0.09	−0.11
1′	3	0.01	0.42	0.46
	3	0.04	0.10	0.10
5	3	−0.65	−0.53	−0.69
5′	3	3.97	3.51	3.58
9	1	−11.26	−13.18	−14.46
	1	−10.85	−12.48	−13.77
9′	3	10.79	9.44	9.72
13	3	−7.68	−8.21	−8.62
13′	3	14.59	13.53	13.62

Table 6. DFT-Calculated Isotropic Coupling Constants of Neutral Radical Formed by Proton Loss at the Methyl Group Attached to Position C13 for Astaxanthin, monoester, and diester

position	number of protons	#Ast•(13)	#mono-Ast•(13)	#di-Ast•(13)
1	3	−0.02	−0.02	−0.02
	3	−0.08	−0.08	−0.06
1′	3	0.01	0.54	0.57
	3	0.05	0.12	0.13
5	3	−0.56	−0.53	−0.38
5′	3	4.47	5.17	4.61
9	3	−1.90	−1.87	−1.54
9′	3	12.20	12.37	12.20
13	1	−17.93	−16.30	−16.25
	1	−17.15	−16.96	−16.99
13′	3	15.93	15.86	15.92

Table 7. DFT-Calculated Isotropic Coupling Constants of Neutral Radical Formed by Proton Loss at Position C3 Followed by Hydroxyl Proton Migration to Carbonyl Group for Astaxanthin and Monoester

position	number of protons	#Ast•(3)b	#mono-Ast•(3′)b
1	3	0.29	0.09
	3	−0.05	0.34
1′	3	0.01	−0.05
	3	0.04	0.68
5	3	−2.14	2.46
5′	3	3.47	−4.75
9	3	−5.09	7.13
9′	3	9.73	−7.45
13	3	−7.73	10.95
13′	3	13.75	−8.45

Table 8. DFT-Calculated Isotropic Coupling Constants of Neutral Radical #mono-Ast•(3)a versus #mono-Ast•(3′)a

position	number of protons	#mono-Ast•(3)a	position	number of protons	#mono-Ast•(3′)a
1	3	−0.54	1	3	0.01
	3	0.2		3	0.04
1′	3	0.02	1′	3	0.05
	3	0		3	−0.42
2	1	22.03	2′	1	18.73
	1	89.58		1	75.7
5	3	0.34	5	3	0.25
5′	3	0.14	5′	3	−3.19
9	3	−0.74	9	3	0.75
9′	3	0.33	9′	3	−2.15
13	3	−0.53	13	3	1.29
13′	3	0.49	13′	3	−1.48

simulated ENDOR fits using DFT-calculated hyperfine coupling constants were used in our previous studies.[6,7,14,22] In the case of carotenoids, a powder ENDOR spectrum lacks the resolution of a solution ENDOR pattern containing spectra of overlapping radicals. We were able, however, to make use of a convenient property of carotenoid radicals, the rotation of the methyl groups at low temperature. At 120 K, the methyl groups rotate very rapidly averaging out the anisotropy and giving isotropic-like spectra. From the cw ENDOR experimental couplings of β carotene radicals formed on silica−alumina, we

were able to calibrate the DFT functions to give an excellent fit.[22] The well-established DFT method was subsequently used to generate the hyperfine coupling constants used in the simulation of various carotenoid radical spectra.[6,7,14] Neutral radicals have been detected at high and low ENDOR frequencies due to much larger DFT-predicted couplings than those of the radical cation. In the Supporting Information, a number of examples have been presented, indicating the limits of the spectral fit.

Figure 8 provides the best attempt at simulating the pulsed Mims ENDOR spectrum of n-octanoic acid diester radicals using the DFT-calculated isotropic β-methyl proton and anisotropic

Table 9. DFT-Calculated Isotropic Coupling Constants of Neutral Radical #mono-Ast•(5) versus #mono-Ast•(5′)

position	number of protons	#mono-Ast•(5)	position	number of protons	#mono-Ast•(5′)
1	3	0.38	1	3	0.10
	3	−0.16		3	0.42
1′	3	0.40	1′	3	0.20
	3	0.10		3	0.64
5	1	−3.25	5	3	2.96
	1	−3.59	5′	1	−4.44
5′	3	3.35		1	−4.78
9	3	−5.44	9	3	8.87
9′	3	9.01	9′	3	−6.07
13	3	−8.2	13	3	12.89
13′	3	12.99	13′	3	−8.51

Table 10. DFT-Calculated Isotropic Coupling Constants of Neutral Radical #mono-Ast•(9) versus #mono-Ast•(9′)

position	number of protons	#mono-Ast•(9)	position	number of protons	#mono-Ast•(9′)
1	3	−0.02	1	3	0.11
	3	−0.09		3	0.44
1′	3	0.42	1′	3	−0.10
	3	0.10		3	−0.02
5	3	−0.53	5	3	3.34
5′	3	3.51	5′	3	−0.60
9	1	−13.18	9	3	9.56
	1	−12.48	9′	1	−12.77
9′	3	9.44		1	−13.38
13	3	−8.21	13	3	13.67
13′	3	13.53	13′	3	−8.40

Table 11. DFT-Calculated Isotropic Coupling Constants of Neutral Radical #mono-Ast•(13) versus #mono-Ast•(13′)

position	number of protons	#mono-Ast•(13)	position	number of protons	#mono-Ast•(13′)
1	3	−0.02	1	3	0.13
	3	−0.08		3	0.59
1′	3	0.54	1′	3	−0.07
	3	0.12		3	−0.02
5	3	−0.53	5	3	4.76
5′	3	5.17	5′	3	−0.51
9	3	−1.87	9	3	12.39
9′	3	12.37	9′	3	−1.74
13	1	−16.30	13	3	15.96
	1	−16.96	13′	1	−16.74
13′	3	15.86		1	−16.10

Figure 8. Pulsed Mims ENDOR spectra of *n*-octanoic acid diester radicals: (a) The black trace is the experimental spectrum produced in activated silica−alumina after UV irradiation; ENDOR parameters: $T = 20$ K, $B = 3465$ G, $\nu = 9.73$ GHz, $\tau = 200$ ns. (b) The red trace is the simulated spectrum using the experimental parameters above and isotropic and anisotropic DFT-calculated couplings of di-Ast•+, #di-Ast•(5), #di-Ast•(9), and #di-Ast•(13) in a 8:14:2:2 ratio. Note: (i) ENDOR lines occur at $\nu_n \pm A/2$, where ν_n is the proton frequency situated in the center of the ENDOR spectrum; (ii) the outer peaks indicated by * are due to the formation of neutral radicals.

α-proton tensors in the Supporting Information in Tables S20 and S22−S24. It shows that the concentration of the neutral radical #di-Ast•(5) exceeds that of the radical cation di-Ast•+ by a factor of 2.

A demonstration of the contributions of the various monoester and diester radicals to the powder ENDOR spectrum has been given in the Supporting Information in Figures S1−S20. The DFT-calculated coupling constant values listed in Tables S9 and S13−S19 (Supporting Information) for monoester and Tables S20 and S22−S24 (Supporting Information) for diester were used in the ENDOR spectral simulations. Usually, the β-protons have very little anisotropy and give rise to narrow and intense lines in powder cw ENDOR spectra, whereas lines from α-protons
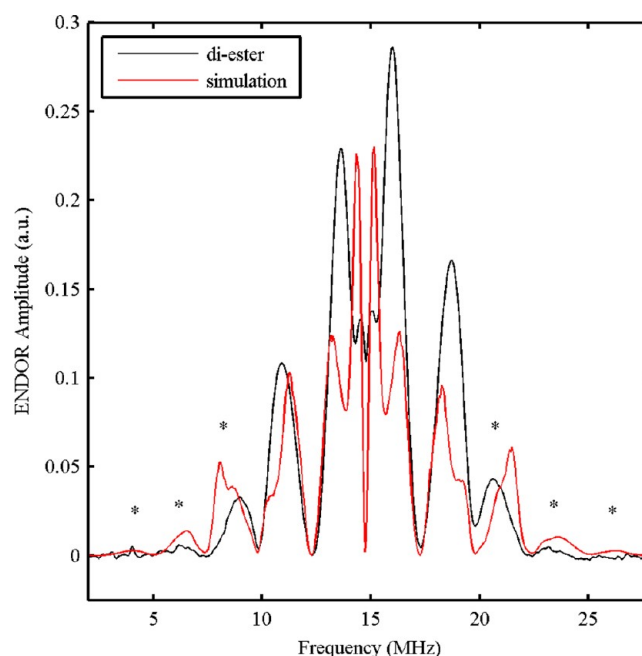
are often broadened and not easily detected.[22] The powder ENDOR spectrum exhibits resolved features which can only be simulated if the full tensor (anisotropic and isotropic components) is used. The fit at the outer edges is crucial because it contains contributions from only the neutral radicals.

The radical cation di-Ast•+ has isotropic couplings of up to 9.6 MHz or ENDOR lines which extend to around 11 and 19 MHz, and anisotropic couplings up to 12 MHz with contributions at around 9 and 21 MHz in the spectrum (see Figure S1 and Table S20 in the Supporting Information). That implies that neutral radicals can be detected as resolved outer peaks below 10 MHz and above 20 MHz due to their larger isotropic couplings (up to 13.71 MHz for #di-Ast•(5) and 13.62 and 15.92 MHz for #di-Ast•(13)).

We attempted to find the ratio in which these neutral radicals contribute to the spectrum, to see whether the concentration of the radical cation di-Ast•+ exceeds that of the preferred neutral radical #di-Ast•(5) and whether neutral radicals #di-Ast•(5), #di-Ast•(9), and #di-Ast•(13) occur equally.

If the simulated ENDOR spectrum for the radical cation diester di-Ast•+ is normalized at 15.2 MHz (Figure S4, in blue, Supporting Information), then the ENDOR line at 19 MHz is weaker than the experimental spectrum. However, if the simulated spectrum for the neutral radical #di-Ast•(5) is normalized at 21 MHz (Figure S4 and S5, in red, Supporting Information), some of the intensity at 18 MHz is recovered.

If the spectrum for the neutral radical #di-Ast•(9) (Figure S8 and S9, in green, Supporting Information) is added and normalized at 21 MHz, some additional intensity at 18−19 MHz is accommodated. Normalizing the spectrum of the neutral radical

#di-Ast[•](9) at 21 MHz (Figure S12 and S13, in purple, Supporting Information) does not contribute substantially to the ENDOR line at 18−19 MHz (Figure S13, Supporting Information). In Figure S16 (Supporting Information), there is a comparison of the experimental ENDOR spectrum and the sum of the radical cation di-Ast[•+] and all three neutrals, #di-Ast[•](5), #di-Ast[•](9), and #di-Ast[•](13), in the ratio of 1:1:1:1 (in green). Peaks at 16−17 MHz and 18−19 MHz are not matched, and the radical cation di-Ast[•+] considerably increases the two split peaks in the middle at 16−17 MHz.

Other combinations have been tried: in Figure S17 (Supporting Information), a combination of 2:2:2 for the sum of the diester neutral radicals and 1:2:2:2 for the radical cation and the three neutral radicals. In Figure S18 (Supporting Information), a combination of 8:2:2:2 shows that more neutral radical #di-Ast[•](5) is needed to fill the line at 11 and 19 MHz. Thus, in Figure 8, a simulation of 8:14:2:2 is given for di-Ast[•+]: #di-Ast[•](5):#di-Ast[•](9):#di-Ast[•](13) which on the low frequency side shows better agreement between the simulated and experimental spectrum. This concentration of neutrals falls in the order of expected radical formation $(5(5') < 9(9') < 13(13'))$, but the diester neutral radical #di-Ast[•](5 or 5′) is twice the concentration of the diester radical cation di-Ast[•+] formed on silica−alumina.

For the monoester, Figure S20 (Supporting Information) gives the simulation for 8:7:7:1:1:1:1:1 (mono-Ast[•+]:#mono-Ast[•](5):#mono-Ast[•](5′):#mono-Ast[•](9), #mono-Ast[•](9′):#mono-Ast[•](13):#mono-Ast[•](13′):#mono-Ast[•](3′OH)) in green compared to the diester in red. The intensity around 11 and 21 MHz is higher due to radicals #mono-Ast[•](5) and #mono-Ast[•](5′) (similar to that when comparing the radicals of diester #di-Ast[•](5) to those of monoester #mono-Ast[•](5) and #mono-Ast[•](5′)). The spectrum was normalized on the low frequency side of the experimental spectrum. The high frequency site has higher intensity due to relaxation effects.

In this study, Mims ENDOR spectra at 9.73 GHz and 3465 G were measured at different delay times τ (τ = 200 ns in Figure 3

and τ = 280 ns in Figure 9) to avoid the "blind-spot" effect. Figure 9 (τ = 280 ns) clearly indicates the outer edges below 10 and above 20 MHz that are due to neutral radicals.

CONCLUSIONS

The diester of astaxanthin reduces the likelihood of neutral radicals forming by proton loss from the C3(3′) end of the carotenoid radical cation which is the preferred proton loss position for the astaxanthin radical cation. Instead, for the diester, the preferred proton loss on the radical cation occurs at the C5(5′) methyl proton. The #di-Ast[•](5 or 5′) exceeds by a factor of 2 or more the concentration of the radical cation di-Ast[•+] stabilized on silica−alumina.

Formation of the monoester of astaxanthin prevents neutral radical formation at the hydrophobic C3 end, and it is formed preferentially at the C3′ hydrophilic end of the carotenoid. The formation of the monoester neutral radical exceeds the formation of the radical cation stabilized on silica−alumina. The EPR and ENDOR spectra for the monoester and diester were superimposable and showed no evidence for the formation of the radical anion which occurred for astaxanthin.

ASSOCIATED CONTENT

⑤ Supporting Information

Isotropic β-methyl proton couplings and anisotropic α-proton tensors (MHz) given in Tables S1−S8 for astaxanthin radicals Ast[•+], #Ast[•](3)a, #Ast[•](3)b, #Ast[•](3OH), #Ast[•](5), #Ast[•](9), and #Ast[•](13), Ast[•−]; in Tables S9−S19 for astaxanthin n-octanoic acid monoester radicals mono-Ast[•+], #mono-Ast[•](3)a, #mono-Ast[•](3′)a, #mono-Ast[•](3)b, #mono-Ast[•](3′OH), #mono-Ast[•](5), #mono-Ast[•](5′), #mono-Ast[•](9), #mono-Ast[•](9′), #mono-Ast[•](13), and #mono-Ast[•](13′); and in Tables S20−S24 for astaxanthin n-octanoic acid diester radicals di-Ast[•+], #di-Ast[•](3), #di-Ast[•](5), #di-Ast[•](9), and #di-Ast[•](13) obtained by DFT calculations. Figures S1−S20 shows simulations of the Mims ENDOR spectra of n-octanoic acid monoester and diester radicals. This material is available free of charge via the Internet at http://pubs.acs.org.

AUTHOR INFORMATION

Notes

The authors declare no competing financial interest.

Figure 9. Mims ENDOR spectra of the astaxanthin monoester and diester at 9.73 GHz and 3465 G, with τ = 280 ns. Note: the outer peaks indicated by * are due to the formation of neutral radicals.

REFERENCES

(1) Mozzo, M.; Dall'Osto, L.; Hienerwadel, R.; Bassi, R.; Croce, R. Photoprotection in the Antenna Complexes of Photosystem II - Role of Individual Xanthophylls in Chlorophyll Triplet Quenching. *J. Biol. Chem.* **2008**, *283*, 6184−6192.
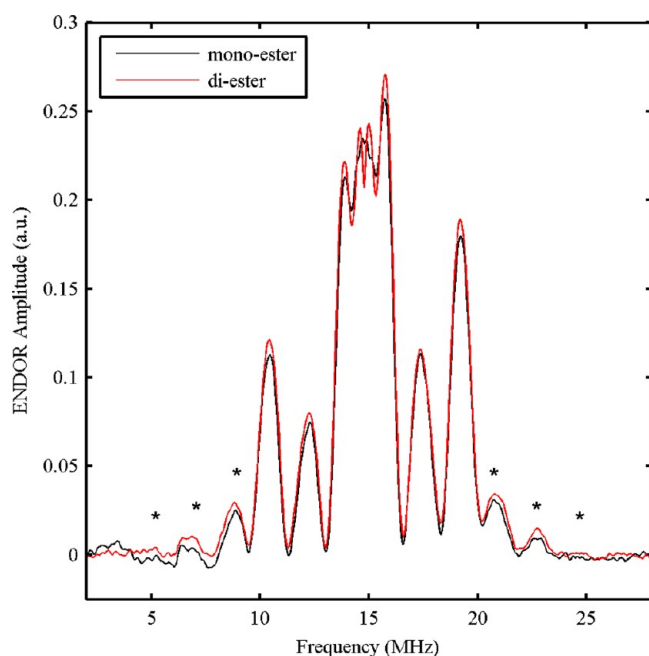
(2) Holt, N. E.; Zigmantas, D.; Valkunas, L.; Li, X. P.; Niyogi, K. K.; Fleming, G. R. Carotenoid Cation Formation and the Regulation of Photosynthetic Light Harvesting. *Science* **2005**, *307*, 433−436.

(3) Ahn, T. K.; Avenson, T. J.; Ballottari, M.; Cheng, Y. C.; Niyogi, K. K.; Bassi, R.; Fleming, G. R. Architecture of a Charge-Transfer State Regulating Light Harvesting in a Plant Antenna Protein. *Science* **2008**, *320*, 794−797.

(4) Avenson, T. J.; Ahn, T. K.; Zigmantas, D.; Niyogi, K. K.; Li, Z.; Ballottari, M.; Bassi, R.; Fleming, G. R. Zeaxanthin Radical Cation Formation in Minor Light-Harvesting Complexes of Higher Plant Antenna. *J. Biol. Chem.* **2008**, *283*, 3550−3558.

(5) Avenson, T. J.; Ahn, T. K.; Niyogi, K. K.; Ballottari, M.; Bassi, R.; Fleming, G. R. Lutein Can Act as a Switchable Charge Transfer Quencher in the CP26 Light-Harvesting Complex. *J. Biol. Chem.* **2009**, *284*, 2830−2835.

(6) Focsan, A. L.; Bowman, M. K.; Konovalova, T. A.; Molnar, P.; Deli, J.; Dixon, D. A.; Kispert, L. D. Pulsed EPR and DFT Characterization of Radicals Produced by Photo-Oxidation of Zeaxanthin and Violaxanthin on Silica-Alumina. *J. Phys. Chem. B* **2008**, *112*, 1806−1819.

(7) Focsan, A. L.; Molnár, P.; Deli, J.; Kispert, L. Structure and Properties of 9′-*Cis* Neoxanthin Carotenoid Radicals by Electron Paramagnetic Resonance Measurements and Density Functional Theory Calculations: Present in LHC II? *J. Phys. Chem. B* **2009**, *113*, 6087−6096.

(8) Kobayashi, M.; Kakizono, T.; Nishio, N.; Nagai, S.; Kurimura, Y.; Tsuji, Y. Antioxidant Role of Astaxanthin in the Green Alga Haematococcus Pluvialis. *Appl. Microbiol. Biotechnol.* **1997**, *48*, 351−356.

(9) Eom, H.; Lee, C. G.; Jin, E. Gene Expression Profile Analysis in Astaxanthin-Induced Haematococcus Pluvialis Using a cDNA Microarray. *Planta* **2006**, *223*, 1231−1242.

(10) Wang, B.; Zarka, A.; Trebst, A.; Boussiba, S. Astaxanthin Accumulation in Haematococcus Pluvialis (Chlorophyceae) as an Active Photoprotective Process Under High Irradiance. *J. Phycol.* **2003**, *39*, 1116−1124.

(11) Hu, Z. Y.; Li, Y. T.; Sommerfeld, M.; Chen, F.; Hu, Q. Enhanced Protection Against Oxidative Stress in an Astaxanthin-Overproduction Haematococcus Mutant (Chlorophyceae). *Eur. J. Phycol.* **2008**, *43*, 365−376.

(12) Guerin, M.; Huntley, M. E.; Olaizola, M. Haematococcus Astaxanthin: Applications for Human Health and Nutrition. *Trends Biotechnol.* **2003**, *21*, 210−216.

(13) Lorenz, T. A Technical Review of Haematococcus Algae, Cyanotech Corporation; http://www.cyanotech.com/pdfs/bioastin/axbul60.pdf (accessed Oct 1, 2012).

(14) Polyakov, N. E.; Focsan, A. L.; Bowman, M. K.; Kispert, L. D. Free Radical Formation in Novel Carotenoid Metal Ion Complexes of Astaxanthin. *J. Phys. Chem. B* **2010**, *114*, 16968−16977.

(15) Fukami, H.; Namikawa, K.; Tomimori, N.; Sumida, M.; Katano, K.; Nakao, M. Chemical Synthesis of Astaxanthin n-Octanoic Acid Monoester and Diester and Evaluation of Their Oral Absorbability. *J. Oleo Sci* **2006**, *55*, 653−656.

(16) Mims, W. B. *Proc. R. Soc. London, Ser. A* **1965**, *283*, 452−457.

(17) Astashkin, A. University of Arizona, http://quiz2.chem.arizona.edu/epr/epr_000006.htm (accessed Oct 1, 2012).

(18) Frisch, M. J.; Trucks, G. W.; Schlegel, H. B.; Scuseria, G. E.; Robb, M. A.; Cheeseman, J. R.; Montgomery, J. A., Jr.; Vreven, T.; Kudin, K. N.; Burant, J. C.; Millam, J. M.; et al. *Gaussian 03*, revision B.02; Gaussian, Inc.: Pittsburgh, PA, 2003.

(19) Frisch, M. J.; Trucks, G. W.; Schlegel, H. B.; Scuseria, G. E.; Robb, M. A.; Cheeseman, J. R.; Scalmani, G.; Barone, V.; Mennucci, B.; Petersson, G. A.; et al. *Gaussian 09*, revision B.1; Gaussian, Inc.: Wallingford, CT, 2009.

(20) Becke, A. D. Density-Functional Thermochemistry. III. The Role of Exact Exchange. *J. Chem. Phys.* **1993**, *98*, 5648−5652.

(21) Lee, C. T.; Yang, W. T.; Parr, R. G. Development of the Colle-Salvetti Correlation-Energy Formula into a Functional of the Electron-Density. *Phys. Rev. B* **1988**, *37*, 785−789.

(22) Gao, Y. L.; Focsan, A. L.; Kispert, L. D.; Dixon, D. A. Density Functional Theory Study of the Beta-Carotene Radical Cation and Deprotonated Radicals. *J. Phys. Chem. B* **2006**, *110*, 24750−24756.

(23) Schafer, A.; Horn, H.; Ahlrichs, R. Fully Optimized Contracted Gaussian-Basis Sets for Atoms Li To Kr. *J. Chem. Phys.* **1992**, *97*, 2571−2577.

(24) Cho, H.; Felmy, A. R.; Craciun, R.; Keenum, J. P.; Shah, N.; Dixon, D. A. Solution State Structure Determination of Silicate Oligomers by Si-29 NMR Spectroscopy and Molecular Modeling. *J. Am. Chem. Soc.* **2006**, *128*, 2324−2335.

(25) http://www.semichem.com/ampac/ampacgui-features.php (accessed Oct 1, 2012).

(26) Jeevarajan, A. S.; Kispert, L. D.; Piekara-Sady, L. An ENDOR Study of Carotenoid Cation Radicals on Silica-Alumina Solid Supports. *Chem. Phys. Lett.* **1993**, *209*, 269−274.